

Article

Influence of Laser Treatment Medium on the Surface Topography Characteristics of Laser Surface-Modified Resorbable Mg₃Zn Alloy and Mg₃Zn1HA Nanocomposite

V. K. Bupesh Raja ^{1,*}, Gururaj Parande ^{2,*}, Sathish Kannan ³, Puskaraj D. Sonawwanay ⁴, V. Selvarani ⁵, S. Ramasubramanian ⁶, D. Ramachandran ¹, Abishek Jeremiah ¹, K. Akash Sundaraeswar ¹, S. Satheeshwaran ¹ and Manoj Gupta ²

¹ Sathyabama Institute of Science and Technology, Chennai 600119, India

² Department of Mechanical Engineering, National University of Singapore, Singapore 117575, Singapore

³ Department of Mechanical Engineering, American University of Sharjah, Sharjah P.O. Box 26666, United Arab Emirates

⁴ School of Mechanical Engineering, Dr. Vishwanath Karad MIT World Peace University, Pune 411038, India

⁵ Department of Chemistry, St. Joseph's Institute of Technology, Chennai 600119, India

⁶ Department of Automobile Engineering, Vels Institute of Science, Technology and Advanced Studies, Chennai 600117, India

* Correspondence: bupesh.v.k@gmail.com (V.K.B.R.); e0010767@u.nus.edu (G.P.)

Abstract: In this study, a Mg₃Zn alloy and a Mg₃Zn1HA nanocomposite were fabricated through disintegrated melt deposition, followed by the hot extrusion process. The specimens were subjected to fiber laser surface modification in air and demineralized water (DM) medium to determine the influence of the laser treatment medium on the microstructure, microhardness, grain size, and surface topography. During the laser treatment, the samples under the water medium produced a lower surface roughness when compared with the air medium. The atomic force microscope (AFM) surface topography scan showed the presence of surface modifications caused by the presence of nanohydroxyapatite (nHA) in the matrix, resulting in a 367.4% and 632.4% increase in the surface roughness (Ra) in the Mg₃Zn1HA nanocomposite when compared with the Mg₃Zn alloy in water and air media, respectively.

Keywords: magnesium alloy; hydroxyapatite; metal matrix composite; resorbable implant; surface modification; topography; laser treatment



Citation: Bupesh Raja, V.K.; Parande, G.; Kannan, S.; Sonawwanay, P.D.; Selvarani, V.; Ramasubramanian, S.; Ramachandran, D.; Jeremiah, A.; Akash Sundaraeswar, K.; Satheeshwaran, S.; et al. Influence of Laser Treatment Medium on the Surface Topography Characteristics of Laser Surface-Modified Resorbable Mg₃Zn Alloy and Mg₃Zn1HA Nanocomposite. *Metals* **2023**, *13*, 850. <https://doi.org/10.3390/met13050850>

Academic Editor: Aleksander Lisiecki

Received: 17 February 2023

Revised: 9 April 2023

Accepted: 19 April 2023

Published: 26 April 2023



Copyright: © 2023 by the authors. Licensee MDPI, Basel, Switzerland. This article is an open access article distributed under the terms and conditions of the Creative Commons Attribution (CC BY) license (<https://creativecommons.org/licenses/by/4.0/>).

1. Introduction

Magnesium and its alloys have emerged as new-age orthopedic fracture fixation implant materials due to virtues such as biocompatibility, resorbability, osteoinductivity, osteoconductivity, angiogenesis, osseointegration, antibacterial and antioxidant properties, and the alleviation of drug-related osteonecrosis in addition to mechanical properties that are similar to human bone [1–12]. However, magnesium in its monolithic form is susceptible to corrosion and wear, which may cause the premature deterioration of the implant [13,14]. To enhance the corrosion and wear properties, magnesium is subjected to alloying, heat treatments, coatings, and surface modifications. The surface topography plays a vital role in the attachment and growth of osteoblastic cells on the surface of the implant [15–17]. Modification of the surface topography through laser surface texturing enhances the wettability and corrosion resistance of bioimplant materials such as Ti6Al4V and Mg alloys [18–21]. Large intermetallic particles—which form microgalvanic couples, leading to the accelerated corrosion of magnesium—are disintegrated, leading to dissolution when subjected to laser ablation during laser processing, thereby reducing the cathodic kinetics [22]. The smooth nanostructured surface layer formed due to laser shock processing (LSP) acts as a barrier to stress corrosion cracking (SCC) [23].

In the ACM720 magnesium–aluminum alloy, the rapid solidification caused by laser treatment increases the solid solubility of aluminum and improves the corrosion resistance through the removal of secondary phase particles from the grain boundaries. The wear resistance and microhardness significantly increase due to solid solution strengthening and grain refinement [24–27]. The wear resistance, surface roughness, and microhardness of the magnesium alloy’s surface treated under laser shock peening tend to improve, owing to the refinement in grain size with an increase in laser energy. High laser energy can be used to develop a functional nanostructured surface topography [28]. Although improvements in the hardness and wear resistance are observed, there is no significant effect on the tensile strength properties post-laser treatment [29].

In many cases, coatings comprising hydroxyapatite on metallic bioimplant materials improve corrosion resistance and cell proliferation by replicating the porous structure of human bones [30–35]. However, there is scant work reported in the literature on the effect of hydroxyapatite as a reinforcement in magnesium and its laser surface modification [12,21].

The laser shock peening of magnesium shows improved grain refinement on the surface and a significant increase in fatigue life due to the development of compressive residual stress in the material surface [36]. The laser shock processing (LSP) of magnesium-based materials indicates the formation of compressive residual stresses, thus improving the fatigue life corrosion resistance and inhibition of bacterial growth on the LSP-treated magnesium surface. These properties are enhanced with the presence of zinc in the magnesium alloy, by the synergetic action of magnesium and zinc, and LSP processing [37].

In the laser ablation of metal matrix composites (MMCs), oxidation of the reinforcing particles is observed [38]. The surface alloying and in situ fabrication of MMCs with a magnesium matrix added with Al_2O_3 and Al particles as a reinforcement through laser surface engineering improved the hardness and wear resistance. The hardness decreased with an increase in the scan speed and laser power [39]. A carbon-dioxide laser is capable of producing a smooth surface, thus giving a polished effect on the magnesium alloy surface. Further, the grain size is refined and hardness increases in the carbon-dioxide laser-processed surface of additive manufactured steel, titanium, Ti6Al4V alloys, magnesium alloys, and AlSi10Mg alloys [40]. The laser shock processing (LSP) of magnesium alloys immersed under water refined the grain size, built up of compressive residual stress, and formed nanostructured crystals, making the alloy immune to stress corrosion cracking (SCC) [41–48].

In high-power diode laser (HPDL) processing, based on the laser parameters, the top surface of the magnesium alloy undergoes laser surface melting where a refined microstructure with homogeneously dispersed secondary phases is observed; the adjacent layer exhibits selective laser surface melting (SLSM) where only the secondary phases are modified [49,50]. The laser-induced periodic surface structure (LIPSS) involving surface melting and texturing improves the hardness and wear resistance. The periodic surface structure of melt regions separated by microgrooves stimulates the cells to attach themselves to the melt zone and repels them from the grooves, thereby stretching them across the grooves [51]. The shape and topography of the grooves are influenced by the type of laser and its parameters [52,53]. The laser treatment of magnesium alloys and nanocomposites exposed to an air medium and immersed under water has yielded grain refinement coupled with the added advantage of incorporating compressive residual stress in the formed nanostructure surface [41–48]. Thus, in this study, the laser treatment of the surface aided in imparting the properties and surface texture favorable for the application of these magnesium materials as orthopedic implants. This experimental investigation was carried out to study the effect of the media on the hardness, surface roughness, and topography as well as the laser interaction with nanohydroxyapatite (nHA) present in the resorbable magnesium alloy and its composite. This study on the influence of laser surface modifications was carried out to enhance the osteoinductivity, osteoconductivity, angiogenesis, and osseointegration of resorbable orthopedic implants through laser processing.

2. Experimental Procedures

2.1. Materials and Processing

Magnesium (Mg) turnings of 99.9% purity sourced from ACROS Organics, Waltham, MA, USA; zinc (Zn) powder with a particle size of 149 μm and 99.9% purity sourced from Alfa Aesar, Ward Hill, MA, USA; and hydroxyapatite (HA) with a particle size of 20 nm and 99.9% purity sourced from MK Impex Corp., Mississauga, ON, Canada, were used as raw materials for the primary processing.

The Mg₃Zn alloys and Mg₃Zn1HA nanocomposites were synthesized using the disintegrated melt deposition (DMD) technique. The raw materials were arranged in a multilayer sandwich form in a graphite crucible and melted to a superheated temperature of 750 °C in the presence of a controlled argon gas environment. For the uniform dispersion of the hydroxyapatite particles in the melt, stirring conditions were optimized at 450 rpm for 5 min. The molten metal was then bottom-poured into a steel mold and disintegrated by two jets of argon gas to obtain cast ingots with a 40 mm diameter. The cast ingots were machined to specific dimensions, soaked at 300 °C for 1 h, and hot-extruded at 250 °C at an extrusion ratio of 20.25:1, yielding an 8 mm rod. Cylindrical discs of 1 mm thickness were cut from the cylindrical rods and processed using a laser and then characterized.

The experiments in the water medium were carried out in a specially designed rig. The rig comprised a stainless-steel disc submerged in demineralized water inside a glass beaker. To facilitate water circulation and the dissipation of heat and removal of debris, holes were drilled in the stainless-steel disc and the disc was made to stand on three legs. The legs were provided with height-adjusting screws to maintain 5 mm water above the magnesium specimen surface (Figure 1) [42].



Figure 1. Liquid laser treatment experimental rig. Reprinted/adapted with permission from Ref. [42] 2021, Elsevier.

A fiber laser (Model No: SH-F10, Meera Laser Solutions, Chennai, India) was used for marking purposes in this study, with a laser wavelength of 1064 nm, pulse repeat frequency of 20–60 kHz, a height of character of 1 mm, and maximum marking speed of 300 characters per second. The laser treatment was carried out using a fiber laser with a power of 10–50 W and a pulse repetition frequency of 25 kHz. An array of dots was made with a laser spot diameter of 0.1 mm and a spot depth of 0.2 mm.

2.2. Characterization

The microstructure and surface morphology of the craters were analyzed using scanning electron microscopy (SEM). The grain size was determined using the comparison

method (ASTM E112). The Vickers microhardness measurements were taken with a load of 0.1 kgf and a dwell time of 10 s. Atomic force microscopy (AFM) analyses of the surface-modified magnesium alloy and nanocomposite specimens processed in air and demineralized water were performed to study the surface texture and roughness of the laser-treated magnesium materials in NT-MDT and modular AFM (Ireland) in the tapping mode using a silicon nitride (Si_3N_4) cantilever. The cantilever was made of a single crystal with an N-type nominal radius of 6 nm and a size of $3.4 \times 1.6 \times 0.3$ mm, which had a resonance frequency of 140–390 kHz (tapping). The surface-scanned images of the magnesium alloy and nanocomposites were flattened using the INTELLIGENT SCANTTM software provided by NT-MDT (NOVA, JEDI Libraries), Tempe, AZ, USA.

3. Results

3.1. Crater Morphology

The craters formed in the air medium exhibited deep gorged walls, with debris on the top surface periphery of the crater, as shown in Figure 2a,c. The craters formed under the water medium were shallow and molten metal residue in the form of a small nugget was created at the bottom of the crater, as shown in Figure 2b,d.

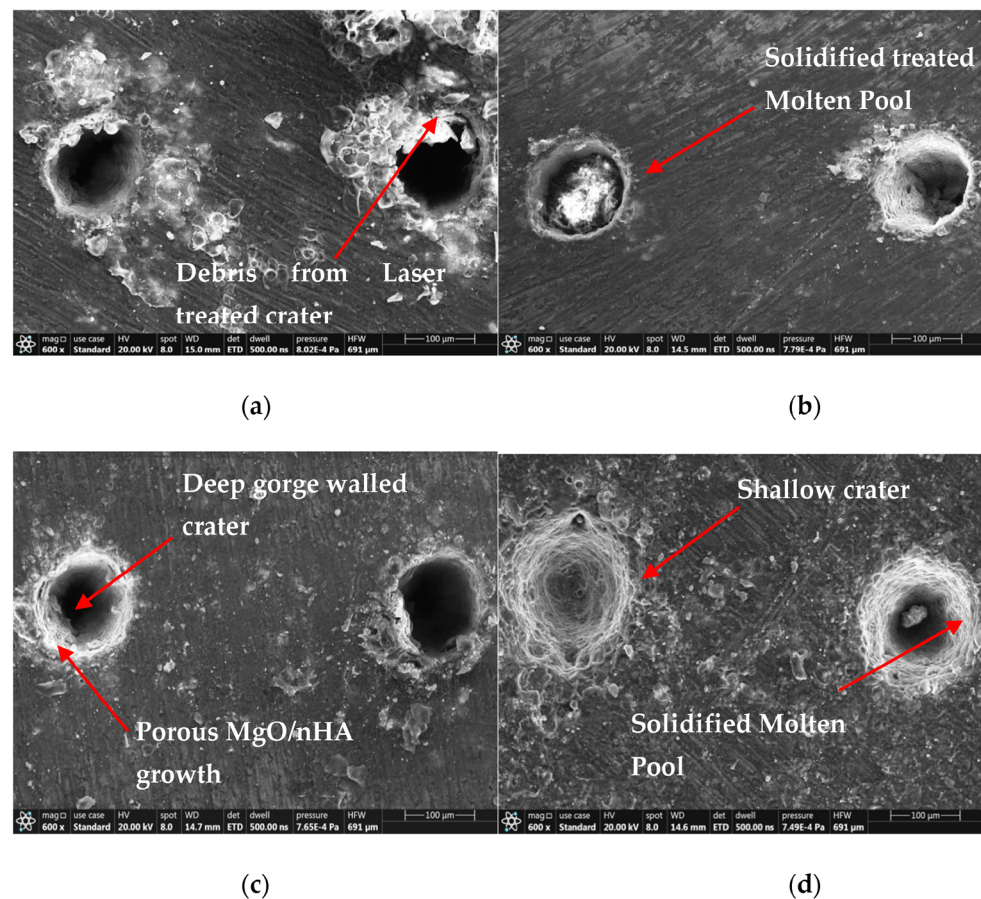


Figure 2. SEM analysis of the top surface of laser-treated magnesium alloy and nanocomposite: (a) Mg₃Zn in air medium; (b) Mg₃Zn in water medium; (c) Mg₃Zn1HA in air medium; (d) Mg₃Zn1HA in water medium.

The craters formed in the air medium were deep and narrow for both the alloy and nanocomposite, as shown in Figure 3a,c. The craters formed under the water medium for both the alloy and nanocomposite were shallow and broad, and the molten metal residue was present inside the crater, as shown in Figure 3b,d. For the Mg₃Zn1HA specimen processed under water, the crater was shallower and broader than the other cases; see Figure 3d.

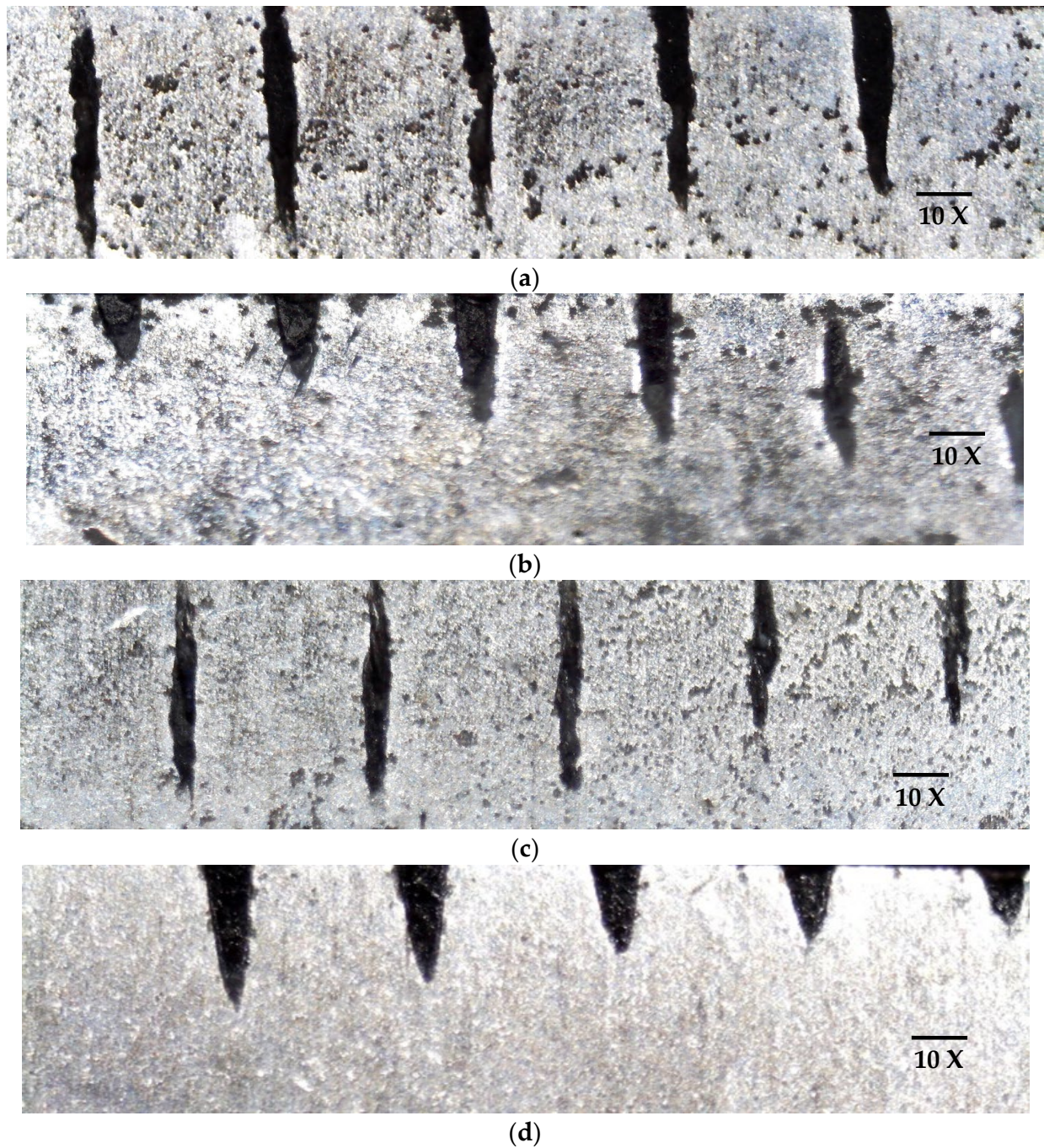


Figure 3. SEM analysis of the cross-sectional surface of laser-treated magnesium alloy and nanocomposite: (a) Mg3Zn in air medium; (b) Mg3Zn in water medium; (c) Mg3Zn1HA in air medium; (d) Mg3Zn1HA in water medium.

The kerf diameter of the craters formed in an air medium in the Mg3Zn alloy was greater than that of the specimens subjected to laser treatment under water. The kerf diameters of the craters formed in the Mg3Zn1HA nanocomposite specimens exhibited the opposite trend, wherein the nanocomposite specimens exhibited a bigger kerf diameter in water than in air. The kerf diameters of the Mg3Zn1HA specimens laser-treated under water showed the biggest kerf diameters in this study, as shown in Figure 4.

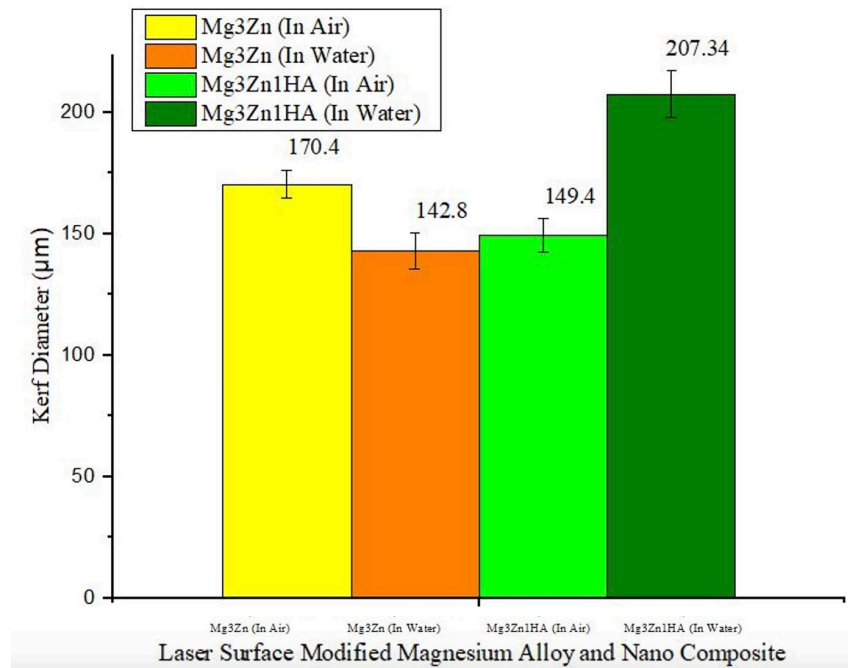


Figure 4. Kerf diameter of craters formed in laser-treated Mg3Zn alloys and Mg3Zn1HA nanocomposites under air and water media.

3.2. Grain Size

The grain size for both the Mg3Zn alloys and Mg3Zn1HA nanocomposites was more refined in the air medium when compared with the water medium. The Mg3Zn grain size for the parent metal was finer in the air. However, for the heat-affected zone (HAZ) and weld zone, there was no visible difference in the grain sizes, as observed in Figure 5. For both the air and water media, the average grain size of Mg3Zn1HA was observed to be finer than Mg3Zn in all the zones, with a slight overlap of standard deviations.

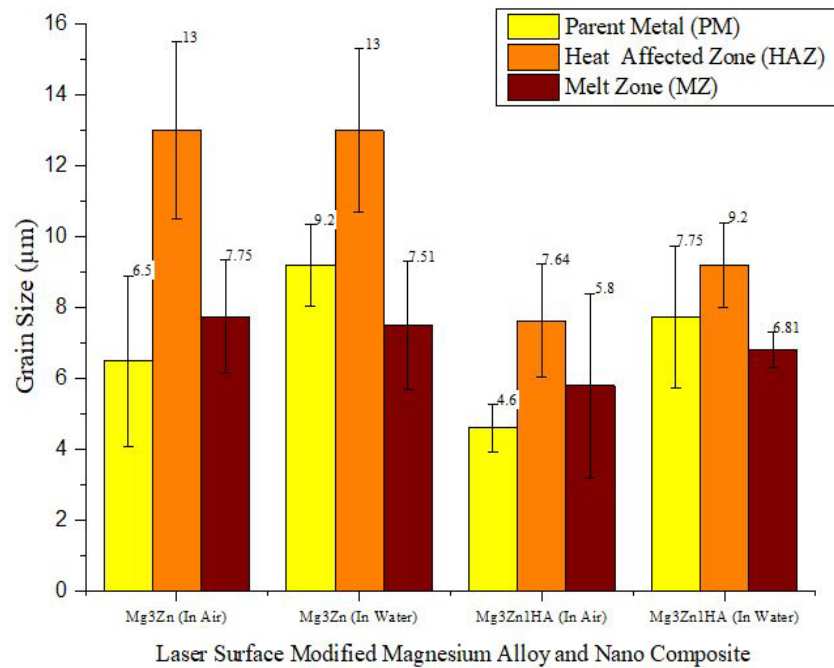


Figure 5. The grain size of Mg3Zn alloys and Mg3Zn1HA nanocomposites subjected to laser treatment under air and water media.

3.3. Microhardness

When we compared the microhardness values, the average values for both the materials in air and water were observed to be similar for the respective zones. Further, the standard deviations overlapped, as shown in Figure 6. With water, the average hardness value for Mg3Zn was the highest for all three zones when compared with Mg3Zn1HA. In the air, the hardness values were similar for all three zones and there was no observable difference.

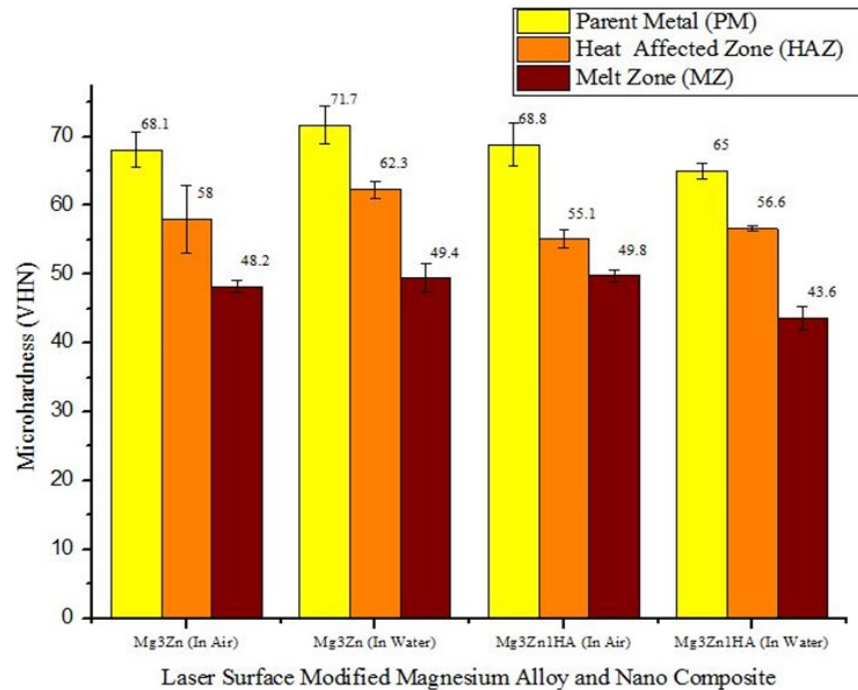


Figure 6. Microhardness of Mg3Zn alloys and Mg3Zn1HA nanocomposites subjected to laser treatment under air and water media.

3.4. Microstructure

3.4.1. Mg3Zn Alloy Laser Treatment under Air Medium

Figure 7 shows the cross-section of the Mg3Zn alloy subjected to laser treatment under an air medium. Figure 7a shows the parent metal zone of the Mg3Zn alloy surface, clearly showing the grain boundaries. The grains were larger and in the range of 6 μm . Figure 7b shows the heat-affected zone of the Mg3Zn alloy, and the micrograph shows a near-equiaxed grain morphology. The heat of the laser treatment resulted in the recrystallization of the parent metal grains of around 13 μm . Some grain growth was observed due to heating. Figure 7c shows the laser-treated zone of the Mg3Zn alloy, and the micrograph of the laser-treated zone shows the melting and fusion of the matrix due to the laser heat.

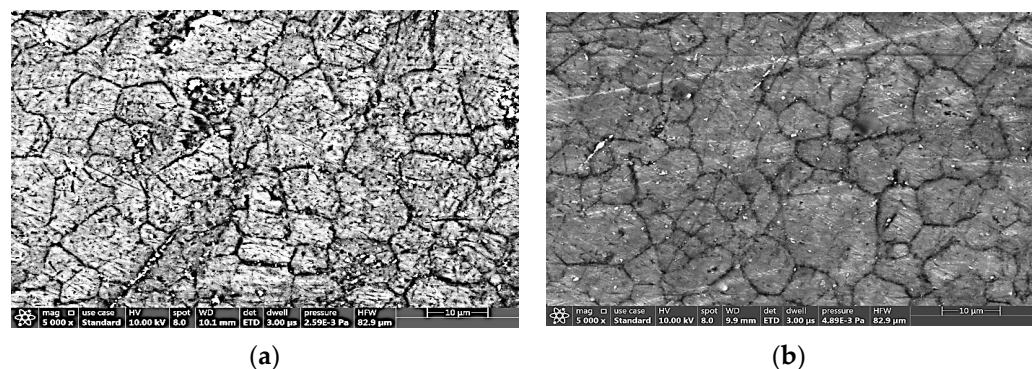
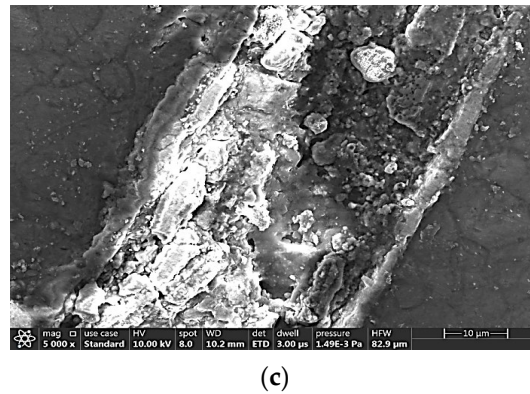


Figure 7. Cont.



(c)

Figure 7. Scanning electron micrographs of Mg3Zn alloy: (a) parent metal (PM); (b) heat-affected zone (HAZ); (c) cross-section of the laser-treated region under air medium.

The energy dispersion spectroscopy of the laser-treated surface detected the presence of magnesium, oxygen, and zinc, as shown in Figure 8. The oxygen detected could be attributed to the possible oxidation of the surface by the action of the laser heat.

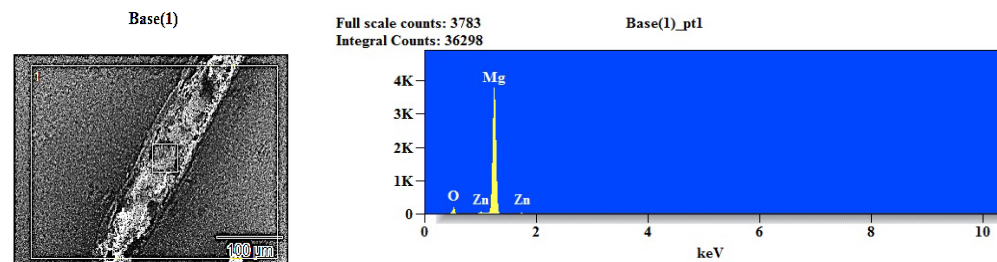
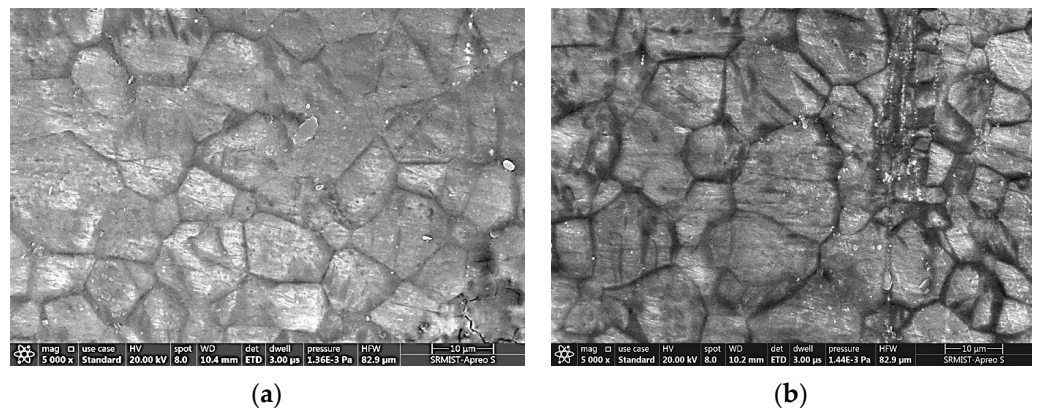


Figure 8. Energy dispersion spectroscopy analysis of Mg3Zn alloy laser-ablated region under air medium.

3.4.2. Mg3Zn Alloy Laser-Ablated under Water Medium

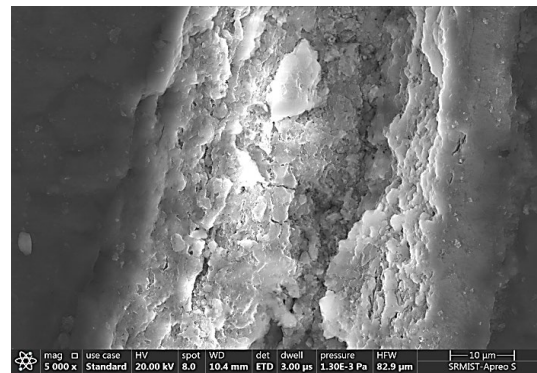
Figure 9 shows the cross-section of the Mg3Zn alloy subjected to laser treatment under the water medium. Figure 9a shows the parent metal zone of the Mg3Zn alloy surface. Figure 9b shows the heat-affected zone of the Mg3Zn alloy surface. The micrograph shows near-equiaxed grains. The heat of the laser resulted in the recrystallization of the parent metal grains of 13 μm . Some grain growth was observed due to heating. Figure 9c shows the laser-treated zone of the Mg3Zn alloy surface. The micrograph of the laser-melted zone shows the melting and fusion of the laser-treated zone due to the laser heat. The laser treatment caused changes in the grains of the material due to the thermal conditions created by the laser. These changes in the grains had implications for the surface roughness of the material.



(a)

(b)

Figure 9. Cont.



(c)

Figure 9. Scanning electron micrograph of Mg3Zn alloy: (a) parent metal (PM); (b) heat-affected zone (HAZ); (c) cross-section of the laser-treated region under water medium.

The energy dispersion spectroscopy of the laser-treated surface detected the presence of magnesium, oxygen, and zinc, and is shown in Figure 10. The pronounced oxygen peaks were due to the oxidation of the surface by the action of the laser heat, as in the air medium.

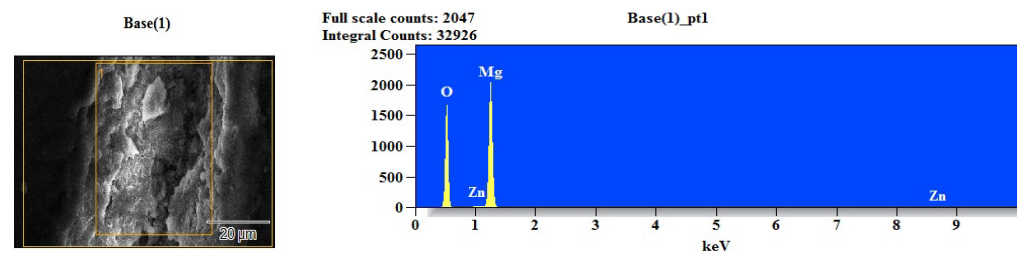


Figure 10. Energy dispersion spectroscopy analysis of Mg3Zn alloy laser-treated region under water medium.

3.4.3. Mg3Zn1HA Nanocomposite Laser Treatment under Air Medium

Figure 11 shows the cross-section of the Mg3Zn1HA nanocomposite subjected to laser treatment under the air medium. Figure 11a shows the parent metal zone of the Mg3Zn1HA nanocomposite. The matrix shows the dispersion of hydroxyapatite particles on the surface. Figure 11b shows the heat-affected zone of the Mg3Zn1HA nanocomposite surface. The micrograph shows the effect of the heat of the laser, resulting in the finer recrystallization of the metal matrix grains. Hydroxyapatite particles were well dispersed in the metal matrix. The recrystallized grains were around 7.6 μm in size in the heat-affected zone. Figure 11c shows the laser-treated zone of the Mg3Zn1HA nanocomposite surface. The micrograph of the laser-treated zone shows the hydroxyapatite particles diffused and sintered into the metal matrix. A thick layer of hydroxyapatite particles sintered to the metal matrix at the crater can be seen. No clear recrystallized grains were observed in this zone.

The energy dispersion spectroscopy of the laser-treated surface detected the presence of magnesium, oxygen, calcium, and zinc, and is shown in Figure 12. The presence of oxygen could be attributed to the oxidation of the surface by the action of the laser heat, leading to the oxidation of magnesium, zinc, aluminum, and calcium.

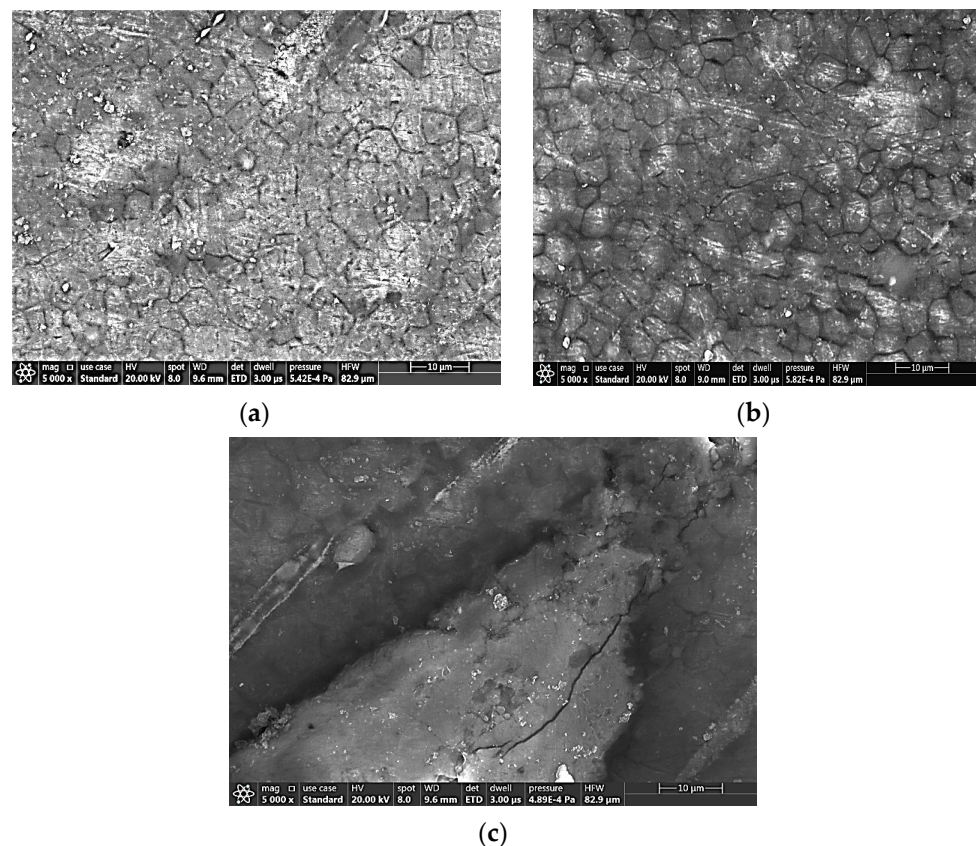


Figure 11. Scanning electron micrograph of Mg₃Zn₁HA nanocomposite: (a) parent metal (PM); (b) heat-affected zone (HAZ); (c) cross-section of the laser-treated region under air medium.

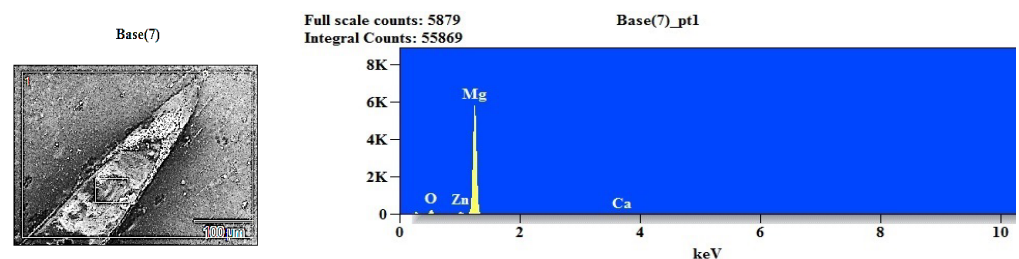


Figure 12. Energy dispersion spectroscopy analysis of Mg₃Zn₁HA nanocomposite laser-treated region under air medium.

3.4.4. Mg₃Zn₁HA Nanocomposite Laser Treatment under Water Medium

Figure 13 shows the cross-section of the Mg₃Zn₁HA nanocomposite subjected to laser treatment under a water medium. Figure 13a shows the parent metal zone of the Mg₃Zn₁HA nanocomposite surface. The micrograph shows the hydroxyapatite particles pinned to the grain boundaries of the metal matrix. Figure 13b shows the heat-affected zone of the Mg₃Zn₁HA nanocomposite surface. The micrograph shows hydroxyapatite particles occupying the grain boundaries of the metal matrix. The heat of the laser resulted in the recrystallization of the parent metal grains. The grain size analysis showed uniform grain sizes of ~10 μm. Figure 13c shows the laser-treated zone of the Mg₃Zn₁HA nanocomposite surface. The micrograph of the laser-melted zone shows that the hydroxyapatite particles diffused and sintered into the metal matrix as a white layer at the sub-surface. The center zone showed no diffusion of the hydroxyapatite particles.

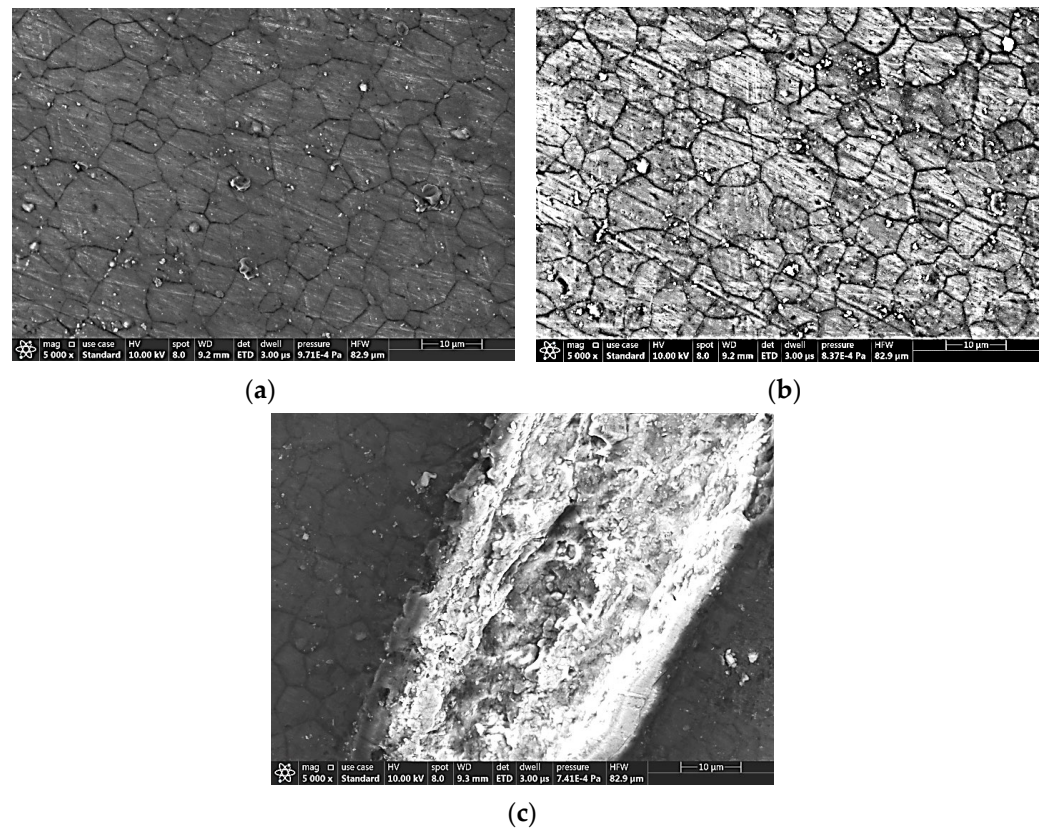


Figure 13. Scanning electron micrograph of Mg3Zn1HA nanocomposite: (a) parent metal (PM); (b) heat-affected zone (HAZ); (c) cross-section of the laser-treated region under water medium.

The energy dispersion spectroscopy of the laser-treated surface detected the presence of magnesium, oxygen, zinc, and calcium, and is shown in Figure 14. The oxygen was due to the oxidation of the surface by the action of the laser heat, as indicated before. Table 1 shows the elemental composition of the laser-treated specimens. In the specimens that were laser-treated under the water medium, it was observed that the content of oxides of magnesium increased drastically due to the exposure to water.

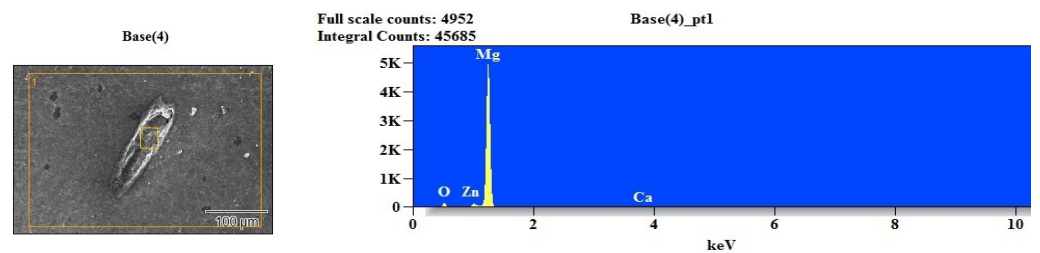


Figure 14. Energy dispersion spectroscopy analysis of Mg3Zn1HA nanocomposite laser-treated region under water medium.

Table 1. Energy dispersion spectroscopy elemental analysis in weight percentage.

Material	O	Mg	Zn	Ca
Mg3Zn (in air)	13.94	83.69	2.37	-
Mg3Zn (in water)	55.25	43.62	1.13	-
Mg3Zn1HA (in air)	13.09	84.36	2.28	0.27
Mg3Zn1HA (in water)	18.43	79.92	1.27	0.38

3.5. Atomic Force Microscopy (AFM)

The AFM analysis data are shown in Table 2. Figures 15–18 show the 3D surface topography AFM images. The laser-treated Mg3Zn magnesium alloy sample treated under the air medium exhibited a maximum particle size of 188.59 nm, an average size of 79.81 nm, and an average roughness and root mean square roughness of 18.01 nm and 23.22 nm, respectively. The laser-treated Mg3Zn magnesium alloy sample treated under the water medium showed a maximum peak-to-peak height of 134.31 nm, the average height on the scanned surface was 94.24 nm, and the average roughness and root mean square roughness were 10.64 nm and 14.24 nm, respectively. The laser-treated Mg3Zn1HA magnesium nanocomposite sample treated under the air medium showed a maximum bump size of 1538.86 nm, with an average cluster formation size of 738.03 nm; the average roughness and root mean square roughness on the surface showed a maximum of 108.39 nm and 146.84 nm, respectively. The laser-treated Mg3Zn1HA magnesium nanocomposite sample treated under the water medium showed a maximum bump size on the surface of 390.87 nm, with an average height profile obtained from a histogram of 251.07 nm; the average roughness and root mean square roughness were obtained as 42.44 nm and 52.31 nm, respectively.

Table 2. AFM surface topographical readings of laser-treated Mg3Zn alloy and Mg3Zn1HA nanocomposite specimens.

Material	Peak-to-Peak (nm)	Ten-Point Height (nm)	Average (nm)	Average Roughness (nm)	Root Mean Square (nm)
Mg3Zn (medium: air)	188.59	85.97	79.81	18.01	23.22
Mg3Zn (medium: water)	134.31	73.70	94.24	10.64	14.24
Mg3Zn1HA (medium: air)	1538.86	766.26	738.03	108.39	146.84
Mg3Zn1HA (medium: water)	390.87	199.40	251.07	42.44	52.31

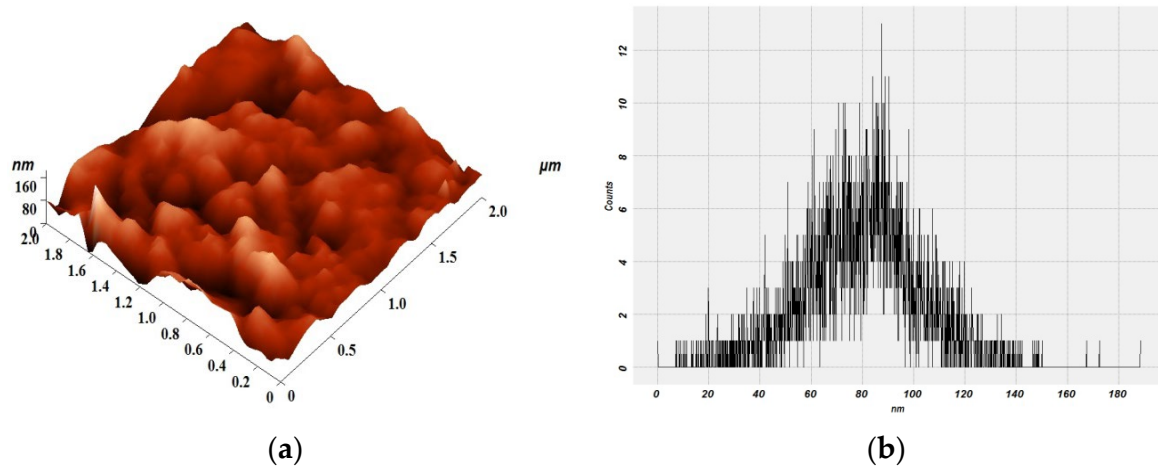


Figure 15. Atomic force microscope results of the laser-treated surface of Mg3Zn alloy under air medium: (a) 3D surface topography; (b) surface histogram.

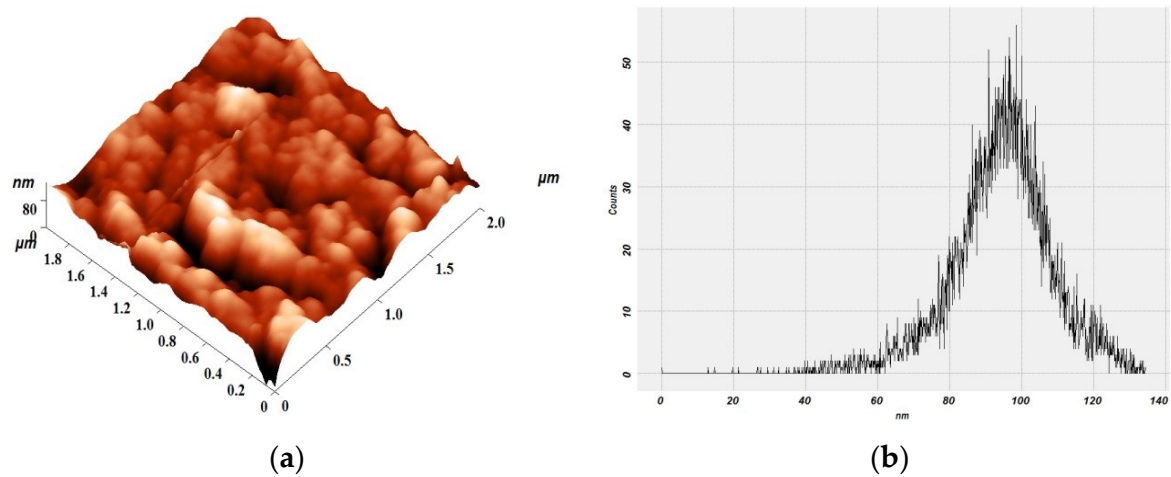


Figure 16. Atomic force microscope results of the laser-treated surface of Mg₃Zn alloy under water medium: (a) 3D surface topography; (b) surface histogram.

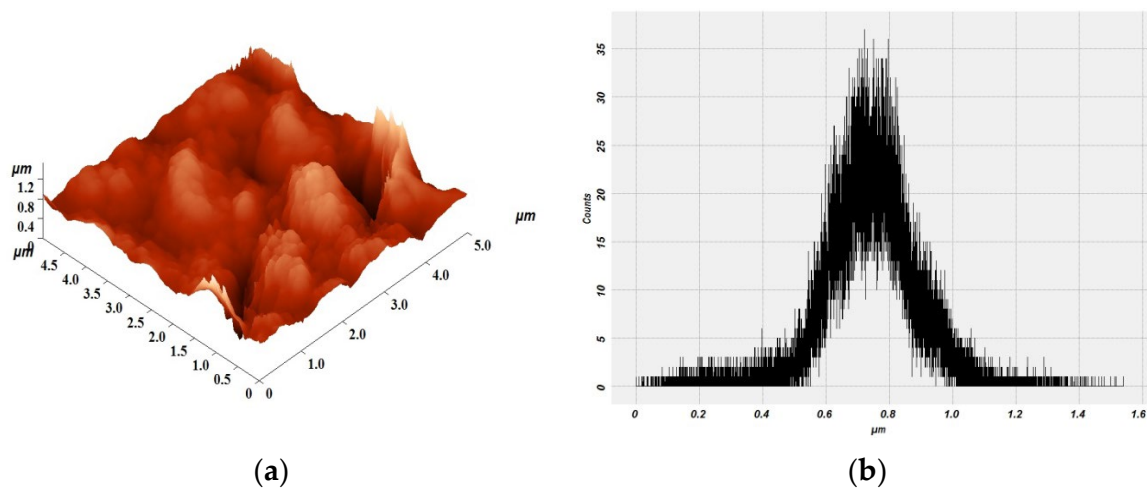


Figure 17. Atomic force microscope results of the laser-treated surface of Mg₃Zn1HA nanocomposite under air medium: (a) 3D surface topography; (b) surface histogram.

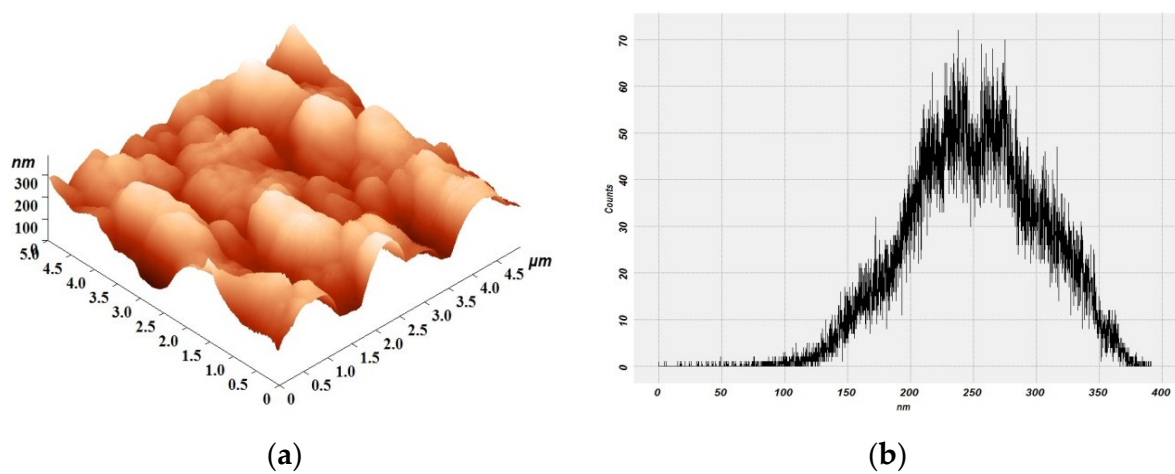


Figure 18. Atomic force microscope results of the laser-treated surface of Mg₃Zn1HA nanocomposite under water medium: (a) 3D surface topography; (b) surface histogram.

4. Discussion

In this experimental investigation, a matrix of craters was created on Mg3Zn alloys and Mg3Zn1HA nanocomposites through laser treatment under air and water media to study the influence of the laser on the surface topography and other properties such as the microhardness, grain size, kerf diameter, macrostructure, and microstructure [16,54–56]. The crater morphology showed the formation of deep gorge-walled craters in the Mg3Zn alloy and Mg3Zn1HA nanocomposite specimens laser-treated in the air medium, which is a typical signature profile in high-energy beams such as laser and electron beams, as shown in Figure 2a,c and Figure 3a,c. Here, the energy of the laser beam was reduced and spent in melting and vaporizing the material on the top surface; as the laser beam reached the bottom, the energy was low and formed a keyhole profile [16]. In Figure 2b,d and Figure 3b,d, the craters were slightly broad and shallow because the dense water medium diffracted the laser and formed a localized cavitation bubble caused by the vaporization of the water and the atomization of the molten metal pool under the influence of the laser plasma formed during the laser ablation. In both the air and water media, the walls of the crater were porous and fluffy due to the formation of pores caused by the escaping of gases upon the explosion or collapse of air or gas pockets formed in the molten metal pool, which spewed out as an atomized eruption [43,57–60].

In the case of laser treatment carried out under the water medium, the entrapment of the molten metal that led to the formation of a nugget at the bottom of the crater was attributed to the backward flow or recoil and negative mass flow of the molten pool caused by the thermocapillary or Benard–Marangoni convection effect, combined with the quenching action of the water medium [60–64]. The hydroxyapatite (HA) nanoparticles present in the nanocomposite sample significantly absorbed the laser energy and enhanced the heat in the laser-treated zone, leading to higher melting, vaporization, and atomization of the molten pool, thus broadening the laser-treated zone and reducing the depth of the crater [61].

In the case of the Mg3Zn alloy specimens, the kerf diameter of the craters formed in the air medium was greater than under water, which was attributed to the confined cavitation bubble encompassing the laser plume under the water medium. In the case of the Mg3Zn1HA nanocomposite specimens, the kerf diameter of the craters formed in water was greater than in air, due to the absorption of the heat of the laser by the HA nanoparticles, enhancing the cavitation bubble and leading to the formation of shallow and broad craters [53], as shown in Figure 4.

The grain size of the laser-treated zone of the Mg3Zn alloy was finer with air than that of the specimens treated in water, as shown in Figure 5. The grain size of the Mg3Zn1HA nanocomposite samples was finer in the air when compared with water, which could be attributed to the absorption of the laser heat by the nano-HA particles and the formation of cavitation bubbles, which sustained the heat slightly longer, leading to a minor increase in the grain size in the water medium. The increase in grain size in the heat-affected zone of all cases of alloys and nanocomposites was due to the soaking of the material with the laser for a longer duration and associated grain growth. When we compared the average grain sizes for each material in air or water, the average values for Mg3Zn1HA were smaller than Mg3Zn. This indicated that the presence of HA refined the microstructure in all the zones. An equiaxed grain morphology is crucial in realizing improvements in mechanical properties, biocompatibility, and the corrosion response.

During extrusion, the ability of nano-HA particles to refine Mg matrix grains can be attributed to the low stacking fault energy of Mg-based materials, resulting in the post-secondary processing of refined grains via hot extrusion [12]. From Figure 6, it is obvious that there was not much influence of the laser treatment medium on the microhardness, which could be attributed to the thermal and metallurgical conditions as well as the elemental constituents present in the specimens during laser treatment. Figure 7a,c and Figure 8a,c show the micrographs of the Mg3Zn alloys laser-treated in air and water media, showing some eutectic precipitates of MgZn₂ at the grain boundaries due to rapid heating and cooling. The micrograph of the laser-treated zone shows the melting and fusion of

the matrix due to the laser heat. The laser plasma within the cavitation bubble rose the temperature of the molten pool; immediately after the collapse of the bubble, the sudden quenching of the metal and subsequent solidification caused the formation of $MgZn_2$. Figure 11a–c show the micrographs of the Mg_3Zn_1HA nanocomposite surface laser-treated under an air medium dispersed with nano-HA particles, and the formation of eutectic precipitates of Mg_2Zn at the grain boundaries.

The presence of HA increases the Gibbs free energy to a higher positive value and decreases the entropy of the reaction because HA absorbs the laser heat energy and causes a non-spontaneous reaction, leading to the formation of Mg_2Zn whereas, in the absence of HA, the reaction happens spontaneously with the actual Gibbs free energy, thus forming stable $MgZn_2$ [65]. Figure 13a–c show the micrographs of the Mg_3Zn_1HA nanocomposite surface laser-treated under a water medium dispersed with nano-HA particles, and the formation of eutectic precipitates of Mg_2Zn at the grain boundaries. Some eutectic precipitates of $MgZn$ -phase $MgZn_2$ were observed at the grain boundaries due to rapid heating and cooling. The micrographs of the Mg_3Zn_1HA nanocomposites revealed a near-uniform distribution of the secondary precipitates and nano-HA particles. It was observed that the secondary precipitates, including the nano-HA particles, displayed a tendency to pin the grain boundaries.

The surface topography of the magnesium alloys with different laser treatments performed under air and in water was examined to obtain an idea about the height of the surface of the laser-treated alloys, as shown in Figures 15–18. The presence of hard nano-HA induced an appreciable increase in the surface roughness than the Mg_3Zn alloy by the formation of nanostructures like nanobumps. The formation of nanobumps was due to the cooling of the particles over the already-cooling substrate. This time delay in the cooling of the surfaces coupled with the Marangoni effect promoted self-organized nanostructuring, with the formation of nanobumps and nanojets [56,60,66].

The height and surface roughness analyzed by AFM on laser-treated alloy surfaces plays an important role in forming a good texture for wettability and the growth of tissue/bone cells on this bioimplant material [33,67]. Surface modifications aid in cell attachment and osteogenesis. Further, the nano-HA caused grain refinement in the Mg_3Zn matrix. Also, the formation of MgO and nano-HA on the surface along with nanobumps induced cell attachment and cell growth. This grain refinement could be attributed to improvements in the mechanical and corrosion behavior of the Mg_3Zn_1HA nanocomposite, thus making it a potential material for a resorbable implant. Based on this approach, microcraters were created in this study wherein these craters provided anchoring to the cells such that the melt zone of the walls of the craters and the melt zone in the crater stimulated the cell attachment. The craters were formed by laser treatment where the material volume boiled and the cavitation bubbles exploded and vaporized. The compositional constituents of the magnesium alloy and composites as well as the microstructure and laser parameters determined the dimensions of the crater. This scheme of surface modification paves the way for the scope of application of Mg_3Zn alloys and Mg_3Zn_1HA nanocomposites in biomedical devices [53].

5. Conclusions

This study was an effort to explore laser treatment as a surface modification route for magnesium-based bioimplant materials. The scope for the nanotexturing of Mg_3Zn alloys and Mg_3Zn_1HA nanocomposites induced by laser treatment media was studied. The highlights of this study were as follows:

1. The Mg_3Zn alloys and Mg_3Zn_1HA nanocomposites fabricated through the disintegrated melt deposition technique were successfully subjected to surface modification through laser treatment using a fiber laser in air and water media.
2. The laser treatment created craters on the surface of the Mg_3Zn alloys and Mg_3Zn_1HA nanocomposites. The laser-treated specimens processed in the water medium exhibited shallow craters, which were attributed to the diffraction of the laser by the water

medium, which also facilitated the removal of debris whereas the laser-treated specimens processed in an air medium exhibited deep gorge-walled craters with geometrically circular profiles at the entry and the presence of ablation debris was observed.

3. The grain size of the laser-treated Mg₃Zn₁HA nanocomposite exhibited refinement when compared with the Mg₃Zn alloy, which was attributed to the nucleation of more new grains caused by the presence of HA nanoparticles in the composite.
4. The surface topography analysis using an atomic force microscope (AFM) showed that the presence of nano-HA yielded a better surface roughness, ideal for cell adhesion and cell growth.

Author Contributions: V.K.B.R.: conceptualization and writing—original draft; G.P.: writing—review and editing; P.D.S.: data curation and writing—review and editing; V.S., S.R. and S.K.: visualization; D.R., A.J., K.A.S. and S.S.: resources; M.G.: project administration. All authors have read and agreed to the published version of the manuscript.

Funding: This research received no external funding.

Institutional Review Board Statement: Not applicable.

Informed Consent Statement: Not applicable.

Data Availability Statement: The data used to support the findings of this study are included within the article and are available from the corresponding author upon request.

Acknowledgments: The authors thank the Materials Division, Department of Mechanical Engineering, National University of Singapore, Singapore, for providing the test specimens for this study. The authors wish to acknowledge the Centre for Nanoscience and Nanotechnology, Sathyabama Institute of Science and Technology, Chennai, Tamil Nadu, India, for providing support for the characterization facilities.

Conflicts of Interest: The authors declare no conflict of interest.

References

1. Shadanbaz, S.; Dias, G.J. Calcium phosphate coatings on magnesium alloys for biomedical applications: A review. *Acta Biomater.* **2012**, *8*, 20–30. [[CrossRef](#)] [[PubMed](#)]
2. Liu, C.; Ren, Z.; Xu, Y.; Pang, S.; Zhao, X.; Zhao, Y. Biodegradable Magnesium Alloys Developed as Bone Repair Materials: A Review. *Scanning* **2018**, *2018*, 9216314. [[CrossRef](#)] [[PubMed](#)]
3. Biber, R.; Pauser, J.; Gefßlein, M.; Bail, H.J. Magnesium-Based Absorbable Metal Screws for Intra-Articular Fracture Fixation. *Case Rep. Orthop.* **2016**, *2016*, 9673174. [[CrossRef](#)] [[PubMed](#)]
4. Thormann, U.; Alt, V.; Heimann, L.; Gasquere, C.; Heiss, C.; Szalay, G.; Franke, J.; Schnettler, R.; Lips, K.S. The biocompatibility of degradable magnesium interference screws: An experimental study with sheep. *BioMed Res. Int.* **2015**, *2015*, 943603. [[CrossRef](#)] [[PubMed](#)]
5. Bai, Y.; Wang, L.; Zhao, L.; Lingling, E.; Yang, S.; Jia, S.; Wen, N. Antibacterial and Antioxidant Effects of Magnesium Alloy on Titanium Dental Implants. *Comput. Math. Methods Med.* **2022**, *2022*, 6537676. [[CrossRef](#)]
6. Zhao, D.; Huang, S.; Lu, F.; Wang, B.; Yang, L.; Qin, L.; Yang, K.; Li, Y.; Li, W.; Wang, W.; et al. Vascularized bone grafting fixed by biodegradable magnesium screw for treating osteonecrosis of the femoral head. *Biomaterials* **2016**, *81*, 84–92. [[CrossRef](#)]
7. Kumar, K.; Gill, R.S.; Batra, U. Challenges and opportunities for biodegradable magnesium alloy implants. *Mater. Technol.* **2017**, *33*, 153–172. [[CrossRef](#)]
8. Zhu, C.; Lv, Y.; Qian, C.; Ding, Z.; Jiao, T.; Gu, X.; Lu, E.; Wang, L.; Zhang, F. Microstructures, mechanical, and biological properties of a novel Ti-6V-4V/zinc surface nanocomposite prepared by friction stir processing. *Int. J. Nanomed.* **2018**, *13*, 1881–1898. [[CrossRef](#)]
9. Liu, Y.; Li, J.; Sun, H.; Cheng, J.; Ren, X.; Jiang, P. Improving ductility of AlSi7Mg alloy by casting-forging process: Effect of deformation degree. *J. Mater. Res. Technol.* **2021**, *14*, 2571–2578. [[CrossRef](#)]
10. Zhu, W.-Y.; Guo, J.; Yang, W.-F.; Tao, Z.-Y.; Lan, X.; Wang, L.; Xu, J.; Qin, L.; Su, Y.-X. Biodegradable magnesium implant enhances angiogenesis and alleviates medication-related osteonecrosis of the jaw in rats. *J. Orthop. Transl.* **2022**, *33*, 153–161. [[CrossRef](#)]
11. Renish, R.R.; Raja, B.V.K.; Sonawwanay, P.D.; Reddy, A.S.; Davanapalli, S.R. An insight into welding of magnesium and its alloys—A review. *AIP Conf. Proc.* **2022**, *2460*, 050007. [[CrossRef](#)]
12. Parande, G.; Manakari, V.; Prasad, S.; Chauhan, D.; Rahate, S.; Wong, R.; Gupta, M. Strength retention, corrosion control and biocompatibility of Mg–Zn–Si/HA nanocomposites. *J. Mech. Behav. Biomed. Mater.* **2019**, *103*, 103584. [[CrossRef](#)]

13. Esmaily, M.; Svensson, J.E.; Fajardo, S.; Birbilis, N.; Frankel, G.S.; Virtanen, S.; Arrabal, R.; Thomas, S.; Johansson, L.G. Fundamentals and advances in magnesium alloy corrosion. *Prog. Mater. Sci.* **2017**, *89*, 92–193. [[CrossRef](#)]
14. Prasad, S.V.S.; Verma, K.; Mishra, R.K.; Kumar, V.; Singh, S. The role and significance of Magnesium in modern day research-A review. *J. Magnes. Alloy.* **2021**, *10*, 1–61. [[CrossRef](#)]
15. Saji, V.S. Electrophoretic (EPD) coatings for magnesium alloys. *J. Ind. Eng. Chem.* **2021**, *103*, 358–372. [[CrossRef](#)]
16. Gedvilas, M.; Indrišiūnas, S.; Voisiat, B.; Stankevičius, E.; Selskis, A.; Račiukaitis, G. Nanoscale thermal diffusion during the laser interference ablation using femto-, pico-, and nanosecond pulses in silicon. *Phys. Chem. Chem. Phys.* **2018**, *20*, 12166–12174. [[CrossRef](#)]
17. Li, G.; Zhang, L.; Wang, L.; Yuan, G.; Dai, K.; Pei, J.; Hao, Y. Dual modulation of bone formation and resorption with zoledronic acid-loaded biodegradable magnesium alloy implants improves osteoporotic fracture healing: An in vitro and in vivo study. *Acta Biomater.* **2018**, *65*, 486–500. [[CrossRef](#)]
18. Patel, D.S.; Singh, A.; Balani, K.; Ramkumar, J. Topographical effects of laser surface texturing on various time-dependent wetting regimes in Ti6Al4V. *Surf. Coat. Technol.* **2018**, *349*, 816–829. [[CrossRef](#)]
19. Wei, D.; Wang, J.; Wang, H.; Liu, Y.; Li, S.; Li, D. Anti-corrosion behaviour of superwetting structured surfaces on Mg-9Al-1Zn magnesium alloy. *Appl. Surf. Sci.* **2019**, *483*, 1017–1026. [[CrossRef](#)]
20. Rakesh, K.R.; Bontha, S.; Ramesh, M.R.; Das, M.; Balla, V.K. Laser surface melting of Mg-Zn-Dy alloy for better wettability and corrosion resistance for biodegradable implant applications. *Appl. Surf. Sci.* **2019**, *480*, 70–82. [[CrossRef](#)]
21. Manne, B.; Thiruvayapati, H.; Bontha, S.; Rangarasaiah, R.M.; Das, M.; Balla, V.K. Surface design of Mg-Zn alloy temporary orthopaedic implants: Tailoring wettability and biodegradability using laser surface melting. *Surf. Coat. Technol.* **2018**, *347*, 337–349. [[CrossRef](#)]
22. Melia, M.A.; Florian, D.C.; Steuer, F.W.; Briglia, B.F.; Purzycki, M.K.; Scully, J.R.; Fitz-Gerald, J.M. Investigation of critical processing parameters for laser surface processing of AZ31B-H24. *Surf. Coat. Technol.* **2017**, *325*, 157–165. [[CrossRef](#)]
23. Ge, M.-Z.; Xiang, J.-Y.; Yang, L.; Wang, J. Effect of laser shock peening on the stress corrosion cracking of AZ31B magnesium alloy in a simulated body fluid. *Surf. Coat. Technol.* **2016**, *310*, 157–165. [[CrossRef](#)]
24. Mondal, A.; Kumar, S.; Blawert, C.; Dahotre, N.B. Effect of laser surface treatment on corrosion and wear resistance of ACM720 Mg alloy. *Surf. Coat. Technol.* **2008**, *202*, 3187–3198. [[CrossRef](#)]
25. Zhang, Y.; Chen, J.; Lei, W.; Xv, R. Effect of laser surface melting on friction and wear behavior of AM50 magnesium alloy. *Surf. Coat. Technol.* **2008**, *202*, 3175–3179. [[CrossRef](#)]
26. Li, Y.; Arthanari, S.; Guan, Y. Influence of laser surface melting on the properties of MB26 and AZ80 magnesium alloys. *Surf. Coat. Technol.* **2019**, *378*, 124964. [[CrossRef](#)]
27. Liu, S.; Hu, J.; Yang, Y.; Guo, Z.; Wang, H. Microstructure analysis of magnesium alloy melted by laser irradiation. *Appl. Surf. Sci.* **2005**, *252*, 1723–1731. [[CrossRef](#)]
28. Ge, M.-Z.; Xiang, J.-Y.; Tang, Y.; Ye, X.; Fan, Z.; Lu, Y.; Zhang, X. Wear behavior of Mg-3Al-1Zn alloy subjected to laser shock peening. *Surf. Coat. Technol.* **2018**, *337*, 501–509. [[CrossRef](#)]
29. Wang, H.; Kalchev, Y.; Wang, H.; Yan, K.; Gurevich, E.; Ostendorf, A. Surface modification of NiTi alloy by ultrashort pulsed laser shock peening. *Surf. Coat. Technol.* **2020**, *394*, 125899. [[CrossRef](#)]
30. Cao, J.; Lian, R.; Jiang, X.; Rogachev, A.V. In vitro degradation assessment of calcium fluoride-doped hydroxyapatite coating prepared by pulsed laser deposition. *Surf. Coat. Technol.* **2021**, *416*, 127177. [[CrossRef](#)]
31. Asl, S.M.; Ganjali, M.; Karimi, M. Surface modification of 316L stainless steel by laser-treated HA-PLA nanocomposite films toward enhanced biocompatibility and corrosion-resistance in vitro. *Surf. Coat. Technol.* **2019**, *363*, 236–243. [[CrossRef](#)]
32. Cotell, C.M.; Chrisey, D.B.; Grabovski, K.S.; Spague, J.A. Pulsed laser deposition of biocompatible thin films. *J. Appl. Biomater.* **1992**, *8*, 87. [[CrossRef](#)]
33. Kalakuntla, N.; Bhatia, N.; Patel, S.; Joshi, S.S.; Wu, T.-C.; Ho, Y.-H.; Dahotre, N.B. Laser patterned hydroxyapatite surfaces on AZ31B magnesium alloy for consumable implant applications. *Materialia* **2020**, *11*, 100693. [[CrossRef](#)]
34. Goto, T.; Kojima, T.; Iijima, T.; Yokokura, S.; Kawano, H.; Yamamoto, A.; Matsuda, K. Resorption of synthetic porous hydroxyapatite and replacement by newly formed bone. *J. Orthop. Sci.* **2001**, *6*, 444–447. [[CrossRef](#)]
35. Vladescu, A.; Braic, M.; Azem, F.A.; Titorencu, I.; Braic, V.; Pruna, V.; Kiss, A.; Parau, A.; Birlik, I. Effect of the deposition temperature on corrosion resistance and biocompatibility of the hydroxyapatite coatings. *Appl. Surf. Sci.* **2015**, *354*, 373–379. [[CrossRef](#)]
36. Praveen, T.; Nayaka, H.S.; Swaroop, S. Influence of equal channel angular pressing and laser shock peening on fatigue behaviour of AM80 alloy. *Surf. Coat. Technol.* **2019**, *369*, 221–227. [[CrossRef](#)]
37. Pacha-Olivenza, M.; Galván, J.; Porro, J.; Lieblich, M.; Díaz, M.; Angulo, I.; Cordovilla, F.; García-Galván, F.; Fernández-Calderón, M.; González-Martín, M.; et al. Efficacy of laser shock processing of biodegradable Mg and Mg-1Zn alloy on their in vitro corrosion and bacterial response. *Surf. Coat. Technol.* **2019**, *384*, 125320. [[CrossRef](#)]
38. Zhang, H.; Zhang, L.; Men, G.; Han, N.; Cui, G. Ablated surface morphology evolution of SiCp/Al composites irradiated by a nanosecond laser. *Surf. Coat. Technol.* **2021**, *429*, 127973. [[CrossRef](#)]
39. Majumdar, J.; Chandra, B.; Mordike, B.; Galun, R.; Manna, I. Laser surface engineering of a magnesium alloy with Al+Al₂O₃. *Surf. Coat. Technol.* **2004**, *179*, 297–305. [[CrossRef](#)]

40. El Hassanin, A.; Obeidi, M.A.; Scherillo, F.; Brabazon, D. CO₂ laser polishing of laser-powder bed fusion produced AlSi10Mg parts. *Surf. Coat. Technol.* **2021**, *419*, 127291. [[CrossRef](#)]
41. Zhang, Y.; You, J.; Lu, J.; Cui, C.; Jiang, Y.; Ren, X. Effects of laser shock processing on stress corrosion cracking susceptibility of AZ31B magnesium alloy. *Surf. Coat. Technol.* **2010**, *204*, 3947–3953. [[CrossRef](#)]
42. BupeshRaja, V.; Parande, G.; Ramachandran, D.; Reddy, A.S.; Gupta, M.; Sonawane, P.D. Studies on surface morphology of under liquid laser ablated magnesium alloy. *Mater. Today Proc.* **2021**, *46*, 1071–1076. [[CrossRef](#)]
43. Kruusing, A. Underwater and water-assisted laser processing: Part 1—General features, steam cleaning and shock processing. *Opt. Lasers Eng.* **2004**, *41*, 307–327. [[CrossRef](#)]
44. Kruusing, A. Underwater and water-assisted laser processing: Part 2—Etching, cutting and rarely used methods. *Opt. Lasers Eng.* **2004**, *41*, 329–352. [[CrossRef](#)]
45. Sano, Y.; Mukai, N.; Okazaki, K.; Obata, M. Residual stress improvement in metal surface irradiation. *Nucl. Instrum. Methods Phys. Res. B* **1997**, *121*, 432–436. [[CrossRef](#)]
46. Itina, T.E. On Nanoparticle Formation by Laser Ablation in Liquids. *J. Phys. Chem. C* **2010**, *115*, 5044–5048. [[CrossRef](#)]
47. Trtica, M.; Stasic, J.; Batani, D.; Benocci, R.; Narayanan, V.; Ciganovic, J. Laser-assisted surface modification of Ti-implant in air and water environment. *Appl. Surf. Sci.* **2018**, *428*, 669–675. [[CrossRef](#)]
48. Wang, C.X.; Liu, P.; Cui, H.; Yang, G.W. Nucleation and growth kinetics of nanocrystals formed upon pulsed-laser ablation in liquid. *Appl. Phys. Lett.* **2005**, *87*, 201913. [[CrossRef](#)]
49. Pulido-González, N.; Torres, B.; Zheludkevich, M.; Rams, J. High Power Diode Laser (HPDL) surface treatments to improve the mechanical properties and the corrosion behaviour of Mg-Zn-Ca alloys for biodegradable implants. *Surf. Coat. Technol.* **2020**, *402*, 126314. [[CrossRef](#)]
50. Liu, C.; Liang, J.; Zhou, J.; Wang, L.; Li, Q. Effect of laser surface melting on microstructure and corrosion characteristics of AM60B magnesium alloy. *Appl. Surf. Sci.* **2015**, *343*, 133–140. [[CrossRef](#)]
51. Zhang, J.; Guan, Y.; Lin, W.; Gu, X. Enhanced mechanical properties and biocompatibility of Mg-Gd-Ca alloy by laser surface processing. *Surf. Coat. Technol.* **2019**, *362*, 176–184. [[CrossRef](#)]
52. Pou-Álvarez, P.; Riveiro, A.; Nóvoa, X.; Fernández-Arias, M.; del Val, J.; Comesaña, R.; Boutinguiza, M.; Lusquiños, F.; Pou, J. Nanosecond, picosecond and femtosecond laser surface treatment of magnesium alloy: Role of pulse length. *Surf. Coat. Technol.* **2021**, *427*, 127802. [[CrossRef](#)]
53. Guan, Y.; Zhou, W.; Li, Z.; Zheng, H. Boiling effect in crater development on magnesium surface induced by laser melting. *Surf. Coat. Technol.* **2014**, *252*, 168–172. [[CrossRef](#)]
54. Voisiat, B.; Gedvilas, M.; Raciukaitis, G. Picosecond Laser 4-beam interference ablation of metal films for microstructuring. In Proceedings of the 29th International Congress on Laser Materials Processing, Laser Microprocessing and Nanomanufacturing, Anaheim, CA, USA, 26–30 September 2010. [[CrossRef](#)]
55. Voisiat, B.; Gedvilas, M.; Indrišiūnas, S.; Račiukaitis, G. Picosecond-laser 4-beam-interference ablation as a flexible tool for thin film microstructuring. *Phys. Procedia* **2011**, *12*, 116–124. [[CrossRef](#)]
56. Indrišiūnas, S.; Voisiat, B.; Gedvilas, M.; Račiukaitis, G. Two complementary ways of thin-metal-film patterning using laser beam interference and direct ablation. *J. Micromech. Microeng.* **2013**, *23*, 095034. [[CrossRef](#)]
57. Wang, J.; Sun, Q.; Zhang, S.; Wang, C.; Wu, L.; Feng, J. Characterization of the underwater welding arc bubble through a visual sensing method. *J. Mater. Process. Technol.* **2017**, *251*, 95–108. [[CrossRef](#)]
58. Amendola, V.; Meneghetti, M. What controls the composition and the structure of nanomaterials generated by laser ablation in liquid solution? *Phys. Chem. Chem. Phys.* **2012**, *15*, 3027–3046. [[CrossRef](#)]
59. Zhigilei, L.V.; Lin, Z.; Ivanov, D.S. Atomistic modeling of short pulse laser ablation of metals: Connections between melting, spallation, and phase explosion. *J. Phys. Chem. C* **2009**, *113*, 11892–11906. [[CrossRef](#)]
60. Bonse, J.; Gräf, S. Maxwell Meets Marangoni—A Review of Theories on Laser-Induced Periodic Surface Structures. *Laser Photon-Rev.* **2020**, *14*, 2000215. [[CrossRef](#)]
61. Rehman, A.U.; Mahmood, M.A.; Pitir, F.; Salamci, M.U.; Popescu, A.C.; Mihailescu, I.N. Mesoscopic computational fluid dynamics modelling for the laser-melting deposition of AISI 304 stainless steel single tracks with experimental correlation: A novel study. *Metals* **2021**, *11*, 1569. [[CrossRef](#)]
62. Mallea, R.T.; Bolopion, A.; Beugnot, J.-C.; Lambert, P.; Gauthier, M. Laser-Induced thermocapillary convective flows: A new approach for noncontact actuation at microscale at the fluid/gas interface. *IEEE/ASME Trans. Mechatron.* **2016**, *22*, 693–704. [[CrossRef](#)]
63. Zhou, X.; Zhong, Y.; Shen, Z.; Liu, W. The surface-tension-driven Benard conventions and unique sub-grain cellular microstructures in 316L steel selective laser melting. *arXiv* **2018**, arXiv:1801.01408. [[CrossRef](#)]
64. Swain, A.; Bhattacharya, A. Effect of Marangoni and Natural Convection during Laser Melting. Available online: https://istam.iitkgp.ac.in/resources/2019/proceedings/Paper_Full/28fullpaper.pdf (accessed on 20 April 2023).
65. Ghosh, P.; Mezbahul-Islam, M.; Medraj, M. Critical assessment and thermodynamic modeling of Mg–Zn, Mg–Sn, Sn–Zn and Mg–Sn–Zn systems. *Calphad* **2011**, *36*, 28–43. [[CrossRef](#)]

66. Nakhoul, A.; Maurice, C.; Agoyan, M.; Rudenko, A.; Garrelie, F.; Pigeon, F.; Colombier, J.-P. Self-organization regimes induced by ultrafast laser on surfaces in the tens of nanometer scales. *Nanomaterials* **2021**, *11*, 1020. [[CrossRef](#)] [[PubMed](#)]
67. Ho, Y.-H.; Vora, H.D.; Dahotre, N.B. Laser surface modification of AZ31B Mg alloy for bio-wettability. *J. Biomater. Appl.* **2014**, *29*, 915–928. [[CrossRef](#)]

Disclaimer/Publisher’s Note: The statements, opinions and data contained in all publications are solely those of the individual author(s) and contributor(s) and not of MDPI and/or the editor(s). MDPI and/or the editor(s) disclaim responsibility for any injury to people or property resulting from any ideas, methods, instructions or products referred to in the content.